Research Square

Preprints are preliminary reports that have not undergone peer review.
They should not be considered conclusive, used to inform clinical practice,
or referenced by the media as validated information.

Potential distribution of Asplenium prolongatum in China and its response to future climate change

Xinyi Liu
Anhui University of Chinese Medicine
Jinchuan Guo
Anhui University of Chinese Medicine
Wanbo Xing
Anhui University of Chinese Medicine
Yan Zhang
Anhui University of Chinese Medicine
Xiao-su Xiang
Anhui University of Chinese Medicine
Qingshan Yang
yqssyx2008@163.com

Anhui University of Chinese Medicine

Research Article

Keywords: bioclimatic envelope, facultative epiphyte, range margins, seasonal moisture, spatial cross-validation

Posted Date: November 26th, 2026

DOI: https://doi.org/10.21203/rs.3.rs-11812678/v1

License: This work is licensed under a Creative Commons Attribution 4.0 International License.
Read Full License

Additional Declarations: No competing interests reported.

Research

Potential distribution of *Asplenium prolongatum* in China and its response to future climate change

Xinyi Liu[1,2,3,4,a], Jinchuan Guo[1,a], Wanbo Xing[1], Yan Zhang[1], Xiao-su Xiang[1] and Qingshan Yang[1,2,3,4]*

[1] Anhui University of Chinese Medicine, College of Pharmacy, Hefei 230012, China

[2] Anhui Province Key Laboratory of Research & Development of Chinese Medicine, Hefei 230012, China

[3] Institute of Conservation and Development of Traditional Chinese Medicine Resources, Anhui Academy of Chinese Medicine, Hefei 230012, China

[4] MOE-Anhui Joint Collaborative Innovation Center for Quality Improvement of Anhui Genuine Chinese Medicinal Materials, Hefei 230012, China

[a]Xinyi Liu and Jinchuan Guo contributed equally to this work and share first authorship.

*Correspondence: Qingshan Yang; yqssyx2008@163.com

Abstract

Asplenium prolongatum is commonly found on forest tree trunks and moist rock surfaces. How its potential suitable area in China will respond to future climate change remains unclear. We fitted maximum entropy (MaxEnt) models to 246 occurrence records using three climate variables and two topographic variables. We evaluated the models with nested spatial cross-validation and assessed future changes using three global climate models (GCMs). Mean temperature of the coldest quarter ranked first in both percentage contribution and permutation importance. Current suitable area covers approximately 1.836 million km², mainly in humid mountains from southwestern to southeastern China; 93.4% remains suitable across all 18 future climate combinations. Under SSP5-8.5 for 2071–2100, we averaged the three continuous GCM projections before thresholding. The resulting suitable area was 15.9% larger than at present, and its area-weighted centroid shifted approximately 91 km northward. Gains were concentrated along the northern margin, with local losses in southern lowlands, coastal areas and parts of Taiwan, China. Nested spatial evaluation yielded a weighted area under the receiver operating characteristic curve (AUC) of 0.900 and a pooled omission rate of 16.7% at the maximum training sensitivity plus specificity threshold. Omission was higher for northern holdouts. The southern mountains contain most of the areas that remain suitable across climates, whereas projections along the range margins warrant field checks.

Keywords: bioclimatic envelope; facultative epiphyte; range margins; seasonal moisture; spatial cross-validation

1 Introduction

Climate change has affected plant phenology and range limits (Parmesan and Yohe 2003; Chen et al. 2011), although responses vary among regions with topography, dispersal and local habitat conditions (Guisan and Thuiller 2005). For plants that grow on moist substrates, warming may alleviate low-temperature constraints at the cold range margin without improving moisture conditions at the warm margin. Fern spores need water to germinate and gametophytes need water for fertilisation, linking fern distributions to seasonal precipitation and local humidity (Krieg and

Chambers 2022). Regional environmental conditions also help explain local fern and lycophyte richness (Weigand et al. 2020). Changes in suitable area for these plants therefore need to be considered alongside the temperature and moisture conditions of the regions affected.

Asplenium prolongatum Hook. is a perennial fern whose rachis often extends into a whip-like, bud-bearing tip. It is found mainly on forest tree trunks and moist rock surfaces at approximately 100–2,000 m elevation (Lin and Viane 2013). It is classified as a facultative epiphyte in Taiwan, China (Hsu and Wolf 2009). Its native range extends from India to south-central and southern Japan and Indochina (Plants of the World Online 2026), and its traditional medicinal use is documented (Royal Botanic Gardens, Kew 2026). Occurrence records from China are dispersed among herbaria, public databases and floras. Bringing these records together with published habitat descriptions allows us to examine how cold-quarter temperature, seasonal moisture and topography relate to the fern's distribution and to identify sites for resurveys and surveys at range margins.

Species distribution models relate occurrence records to environmental gradients and allow comparisons of potential suitability across climates (Guisan and Thuiller 2005). MaxEnt can be used where presence records are available but systematic surveys of absences are lacking (Phillips et al. 2006; Elith et al. 2011). Previous work used this approach to examine climatic suitability and conservation patterns for a fern in China (Guo et al. 2026). Model complexity, predictor collinearity and background extent can all affect predictions (Warren and Seifert 2011; Dormann et al. 2013; Merow et al. 2013). Combining spatial holdout evaluation with projections from several climate models allows agreement within and along the edges of the main suitability belt to be assessed.

We compared current and future potential suitability for *A. prolongatum* in China, focusing on whether the southern mountain belt persists and whether projected changes at the northern margin agree with those in the south. Using spatial holdouts and alternative occurrence treatments and model settings, we examined where predictions were consistent within and along the edges of the belt. We also compared the collection localities of two Anhui specimens not used to fit the models with the current suitability map to examine their spatial relationship to predicted patches in southern Anhui.

2 Materials and Methods

2.1 Study area and spatial domains

We calibrated and projected the main model across China's land area to support national resource surveys and area estimates. This domain covers the environmental gradients represented by the occurrence records from China. The area accessible to the species depends on its dispersal history and geographical connectivity (Barve et al. 2011). We aligned the environmental layers to a WGS84 grid at 2.5 arc-min resolution. After excluding sea cells and cells with missing predictor values, the analysis retained 545,461 cells covering approximately 9.344 million km². To assess the effect of

calibration extent, we dissolved 500-km buffers around the 246 modelling records and intersected them with the national domain to obtain the alternative calibration domain, M500.

We summed ellipsoidal grid-cell areas using NumPy 2.4.3. Area-weighted geographical centroids were calculated in the ESRI:102012 projection, and distances between them were measured along geodesics on the WGS84 ellipsoid. Coordinate transformations and geodesic distances were calculated in PyProj 3.7.2. All analyses used the same national grid and cell alignment. Administrative boundaries and the South China Sea inset used the cartographic layers of Guo et al. (2026) for display; they did not define the environmental grid mask.

2.2 Occurrence records and spatial filtering

We verified the accepted name and nomenclature using Plants of the World Online (POWO), the International Plant Names Index (IPNI) and the GBIF Species API (taxon key 4256698; Plants of the World Online 2026; International Plant Names Index 2026; GBIF.org 2026). Occurrence records came from the Global Biodiversity Information Facility (GBIF), the Chinese Virtual Herbarium (CVH), the National Specimen Information Infrastructure (NSII), voucher specimens, floras and publications (Chinese Virtual Herbarium 2026; National Specimen Information Infrastructure 2026). Online Resource 2 provides the GBIF records from all years, query URLs and access dates.

Combining the sources and removing duplicates yielded 301 unique coordinates, including one in Anhui. After excluding two incorrectly georeferenced coordinates, 11 with missing environmental values and the Anhui coordinate, 287 remained. Retaining one record per 2.5 arc-min cell yielded 246 records for the main analysis. The retained set comprised 58 records with specimen or image evidence (E1), 53 with traceable vouchers or catalogue numbers (E2) and 135 curated coordinate records (E4). The 111 E1 and E2 records, dated 1980–2026, formed the subset for the occurrence-evidence sensitivity analysis. The current climate baseline was 1981–2010.

Some historical Anhui records confused *A. prolongatum* with *Asplenium incisum* Thunb. Most of the 28 NSII specimen images examined represented *A. incisum*. The associated historical records were excluded from the national model. Two verified Anhui specimens of *A. prolongatum* were used for the post-model spatial comparison: JSL5601 (duplicate sheets CSH0152438, HZU 60160998 and HZU 60168794), collected in August 2017 at Tianzuo Maze in Guniujiang Scenic Area, Dayan Township, Shitai County; and 341024170424876LY, collected in April 2017 at Yinjiangyuan, Xiangdong Village, Likou Town, Qimen County. Collection information is provided in Online Resource 2.

Spatial thinning at 20 km retained 168 records, which were used to assess the effect of increasing the thinning distance (Boria et al. 2014). The target-group background used 194,689 georeferenced voucher records of non-target ferns from GBIF in China, excluding *A. prolongatum*. We applied

three smoothing scales (σ = 6, 12 and 24 cells, corresponding to approximately 28, 55 and 110 km) to generate sampling-effort surfaces. After normalisation, weights were bounded between 0.01 and 20 and supplied to MaxEnt as bias files. The main model used 10,000 uniformly sampled background cells. The three effort surfaces were used to assess the effect of correcting for sampling bias (Phillips et al. 2009). Table 1 summarises record processing and Fig. 1 shows the modelling localities.

2.3 Predictor selection

The candidate dataset comprised 104 climate, topography, soil, radiation, UV-B and vegetation layers. Screening considered data completeness, ecological relevance and availability for future scenarios, with emphasis on temperature, seasonal moisture and mountain topography. Across cells with valid values for all layers in the national domain, we computed Pearson correlations with NumPy corrcoef and variance inflation factors (VIFs) from the diagonal of the inverse correlation matrix. Retained combinations were required to have $|r| < 0.8$ and VIF < 4. We compared BIO04 with BIO11 within a six-variable set comprising BIO04, BIO11, BIO15, BIO17, elevation and slope, then fixed the five-variable set before parameter calibration. Climate-only and climate-plus-elevation sets were used to assess sensitivity to predictor structure. Online Resource 2 contains the predictor inventory, screening sequence and correlation results (S2_Predictor_Ledger, S2_Screening_Summary, S2_6var_Correlation and S2_6var_VIF); the calculations are detailed in Methods S3 of Online Resource 1.

Current BIO11, BIO15 and BIO17 layers came from CHELSA v2.1 climatologies for 1981–2010 (Karger et al. 2021), and future climate layers came from CHELSA CMIP6 (Brun et al. 2022). Elevation came from WorldClim v2.1 (Fick and Hijmans 2017; WorldClim 2026). We derived slope with the Horn 3 × 3 algorithm (Horn 1981) and used a latitude-corrected calculation for comparison. Current analyses used the aligned national layers. We used Rasterio 1.5.0 to resample future continuous climate layers by bilinear interpolation to the same grid, matching layer extent, resolution and cell alignment. Table 2 gives the retained predictors and their treatment in future projections; Online Resource 2 and Online Resource 3 document their sources and processing.

2.4 Parameter selection and spatial evaluation

We fitted the models using R 4.6.0, archived kuenm 1.1.10 source code and MaxEnt 3.4.4 (Java 1.8.0_391), and computed spatial summaries in Python 3.14.3. The kuenm functions were loaded from the archived R source using sys.source. Software versions and analytical roles are listed in Methods S3 of Online Resource 1. For full-dataset parameter selection, the 246 records were split into 185 calibration and 61 evaluation records using seed 20260813. Regularisation multipliers (RMs) of 0.1, 0.5, 1.0, 1.5, 2.0, 2.5, 3.0, 3.5 and 4.0 were paired with all 31 non-empty combinations of linear (L), quadratic (Q), product (P), threshold (T) and hinge (H) features, giving 279

configurations. Following the kuenm workflow (Cobos et al. 2019), partial ROC (pROC) analysis used 500 bootstrap iterations, each sampling 50% of the evaluation records. We retained models with $p < 0.05$ and evaluation omission ≤5% at kuenm's E = 5% training-omission threshold and ranked them by the small-sample-corrected Akaike information criterion (AICc). The lowest-AICc configuration was selected. AICc was calculated using raw predictions for all records, the sample size n = 246 and the number of non-zero lambda coefficients K. This random split screened the candidate configurations; performance was evaluated separately by tenfold and spatial cross-validation. The mapping configuration used RM = 2 and QP features.

We divided the 246 records at the median longitude and latitude into four outer spatial folds: southwest, southeast, northwest and northeast, with 47, 76, 76 and 47 records, respectively (Muscarella et al. 2014; Roberts et al. 2017). We held out one fold for spatial testing and used the other three for tuning and fitting. Within those three folds, we randomly allocated 75% of records to inner training and 25% to inner evaluation and compared all 279 configurations again. The inner split was not spatially blocked; the four seeds were 20260831–20260834. We refitted each selected configuration to its outer training set and evaluated it on the held-out spatial fold. The five predictors were held fixed across folds, so the nested selection concerned model complexity.

We evaluated performance using the area under the receiver operating characteristic curve (AUC), omission at the maximum training sensitivity plus specificity threshold (MTSPS) and at the 10th-percentile training presence threshold (P10), and a grouped Boyce index (Boyce et al. 2002; Hirzel et al. 2006). Quantiles of the background predictions defined 10 bins. We calculated the ratio of observed to expected occurrence frequency (P/E) for each bin and used the Spearman correlation between bin midpoints and P/E as the Boyce index. Each spatial fold's MTSPS and P10 thresholds were determined from its outer training model and records. We weighted AUC by test sample size, pooled omission counts across folds and averaged fold-specific Boyce indices.

Mapping used a random tenfold ensemble with RM = 2 and QP features. We projected the 10 fold-specific logistic predictions onto the national grid and averaged them. The settings were 10,000 background cells, 500 maximum iterations and a convergence threshold of 1×10^{-5}; extrapolation and clamping were disabled. In addition to nested tuning, we evaluated the fixed RM = 2, QP configuration on the same outer spatial folds to assess the mapping configuration. Random-tenfold, fixed-QP spatial and nested-tuning results were summarised separately. Model objects and threshold sources are listed in Methods S1 of Online Resource 1; fold assignments, seeds and candidate results are in Online Resource 2.

2.5 Current suitability classes and predictor importance

We estimated current suitability by averaging the 10 RM = 2, QP logistic surfaces. The main binary classification used the mean tenfold MTSPS threshold of 0.2116, which balances sensitivity to training presences with specificity relative to background cells. We used the P10 threshold of 0.2742 and the equal-sensitivity-and-specificity threshold of 0.3052 to assess how area estimates varied with the threshold. Scores above MTSPS were divided into three equal-width classes: low, moderate and high suitability. Percentage contributions, permutation importance, response curves and jackknife gains were summarised from the same 10 fold-specific models.

2.6 Future projections, GCM differences and environmental similarity

We used three global climate models (GCMs), GFDL-ESM4, IPSL-CM6A-LR and MRI-ESM2-0, under the low-emissions Shared Socioeconomic Pathway SSP1-2.6 and the high-emissions pathway SSP5-8.5 for 2011–2040, 2041–2070 and 2071–2100 (O'Neill et al. 2016). The GCMs come from different modelling centres and provide the required CHELSA scenario data for comparing projections (Eyring et al. 2016; Yukimoto et al. 2019; Boucher et al. 2020; Dunne et al. 2020). Three climate predictors varied with scenario; elevation and slope were held constant. For each GCM we first averaged the 10 fold-specific logistic projections. For each SSP and period, we then averaged the three continuous GCM surfaces with equal weights and applied the binary threshold of 0.2116 to obtain the main area estimates. We also classified each GCM separately to compare agreement among them.

We overlaid current and future binary maps to identify stable, lost and newly suitable areas. A cell was considered stable across the 18 future combinations if it was suitable at present and under every combination of three GCMs, two SSPs and three periods. Area-weighted centroids were calculated using the main MTSPS threshold. We computed multivariate environmental similarity surfaces (MESS) using a custom NumPy implementation, with the 545,461 national cells having valid values for all five current predictors as the reference. For each GCM, MESS was the minimum similarity score across the five predictors (Elith et al. 2010). For any SSP and period, a cell was outside the reference environmental range if at least one GCM yielded negative MESS. The conservative reclassification removed these cells from the future suitable area only. The paired common-support comparison applied the non-negative MESS mask to both current and future maps.

2.7 Calibration domain and sensitivity analyses

We reassessed the 279 configurations within M500, selected RM = 1 with LQ features and fitted a tenfold ensemble. Current and future suitability were the arithmetic means of the 10 fold-specific predictions; binary classification used the mean tenfold MTSPS threshold of 0.23901. For spatial evaluation we trained the fixed RM = 1, LQ configuration on three quadrant folds and tested on the

fourth. The background remained the M500 domain defined in advance from all 246 records. We summarised change within M500 and across the national projection domain, then performed a paired MESS common-support comparison referenced to the M500 background. Fold thresholds and reporting extents are given in Methods S2 of Online Resource 1.

We compared model structures using two fitting designs. We fitted tenfold ensembles for the RM = 2, LQP model with ΔAICc < 2 and for the climate-only and climate-plus-elevation QP models, applying each ensemble's mean tenfold MTSPS threshold. Each of the four configurations selected by the outer spatial folds (LT, P, LQ and QPT) was fitted as a single model using all 246 records and compared with an RM = 2, QP model fitted to the same records. These all-record models used their respective MTSPS thresholds and were projected under all three GCMs for SSP5-8.5 in 2071–2100 to assess the effect of parameter choice on forecasts. Separate tenfold ensembles were fitted to the E1+E2 subset, the 20-km-thinned records and the three target-group backgrounds, and projected across all 18 future combinations. Configurations and comparison baselines are given in Methods S1 of Online Resource 1 and in Online Resource 2.

2.8 Translation assistance

The authors used OpenAI Codex to translate the Chinese manuscript into English. The authors are responsible for the final text.

3 Results

3.1 Predictor selection and model performance

The six-variable set had a maximum VIF of 12.417. Excluding BIO04 left BIO11, BIO15, BIO17, elevation and slope, reducing maximum |r| to 0.636 and maximum VIF to 2.049. Of the 279 candidate configurations, 25 met both the $p < 0.05$ and evaluation omission ≤5% criteria. The RM = 2, QP model had the lowest AICc; the RM = 2, LQP model had a ΔAICc of 1.69.

For the fixed RM = 2, QP configuration, test AUC in random tenfold cross-validation was 0.922 ± 0.021. The spatial evaluation gave a weighted AUC of 0.898 and pooled omission rates of 13.0% at MTSPS and 29.3% at P10 (Table 3; Fig. 2).

Nested tuning selected different configurations in the four outer training sets. Weighted spatial AUC was 0.900, pooled omission rates at MTSPS and P10 were 16.7% and 34.6%, respectively, and the mean grouped Boyce index was 0.734. The northwest fold had the highest P10 omission (55.3%) and the northeast fold had the highest MTSPS omission (27.7%). Table 3 gives the configuration and evaluation results for each fold.

Current maps from the E1+E2 subset, 20-km thinning and the three target-group backgrounds had correlations of 0.971–0.995 and Jaccard indices of 0.870–0.963 against the main model. All

treatments projected a net gain in suitable area by the end of the century under SSP5-8.5, ranging from 12.9% to 19.4% (Table S1; Fig. S8; Online Resource 1).

3.2 Principal predictors and current suitable area

Of the five predictors, BIO11 ranked first in percentage contribution (55.85%) and permutation importance (46.68%). Contributions of BIO15 and BIO17 were 19.45% and 19.04%, respectively. Elevation contributed 3.50% but had a permutation importance of 25.52%; slope ranked low on both measures (Fig. 3; Table S2 in Online Resource 1). Response curves and jackknife results are shown in Figs. S1 and S2 (Online Resource 1). Latitude-corrected slope was strongly correlated with the slope layer used in modelling ($r = 0.996$, RMSE = 0.229°). Calculations and comparisons are provided in Online Resource 3.

At the MTSPS threshold, current suitable area covered approximately 1,836,000 km², or 19.65% of the valid domain. Low, moderate and high suitability covered approximately 1,257,100, 541,900 and 37,000 km², respectively. Low suitability accounted for 68.5% of total suitable area, and moderate and high suitability together covered 578,900 km², or 31.5%. The logistic suitability class boundaries were 0.2116, 0.4744 and 0.7372 (Table 4). Suitable areas formed a broad belt through the humid mountains of southern China. Highly suitable patches were concentrated in Yunnan–Guizhou, southern Sichuan–Chongqing, Hunan–Jiangxi, the Nanling–Wuyi Mountains and Fujian–Zhejiang. Southern Anhui contained patches of low and moderate suitability, and suitable areas occurred in parts of Taiwan, China (Fig. 4).

The representative point for the Shitai collection and the Qimen specimen locality both fell within predicted suitable patches in southern Anhui. Their current suitability scores, 0.415 and 0.637, respectively, were above the MTSPS threshold. All cells in the 5 × 5 neighbourhood around the Qimen locality met the suitability threshold; 60% were moderately or highly suitable.

3.3 Future suitable area and centroid shifts

We averaged the three continuous GCM projections and applied the main threshold to distinguish suitable and unsuitable areas. Relative to the current baseline, suitable area increased in all six SSP–period combinations. For 2011–2040, 2041–2070 and 2071–2100, the increases were 2.5%, 6.8% and 6.9% under SSP1-2.6 and 2.8%, 8.8% and 15.9% under SSP5-8.5. At the end of the century under SSP5-8.5, approximately 1.7956 million km² remained suitable, 332,500 km² became newly suitable and 40,400 km² became unsuitable. The P10 and equal-sensitivity-and-specificity thresholds gave end-century increases of 21.8% and 26.0%, respectively. Gains were concentrated along the northern margin, from Sichuan–Chongqing towards Hubei and from Anhui towards the lower Yangtze. Losses were smaller and scattered across Hainan, the warm, humid southern lowlands, the

southeastern coast and Taiwan, China (Fig. 5). Scenario-specific maps are shown in Fig. S6 (Online Resource 1).

The current area-weighted centroid of suitable area was at 110.2°E, 26.6°N. By the end of the century it shifted about 35 km to 110.3°E, 26.9°N under SSP1-2.6 and about 91 km northward to 110.2°E, 27.4°N under SSP5-8.5 (Fig. 6). The centroid positions differed among GCMs, thresholds and model structures.

By the end of the century under SSP5-8.5, suitable area increased by 16.3%, 13.8% and 17.1% for the LQP, climate-only and climate-plus-elevation tenfold ensembles, respectively. We fitted each of the four configurations selected in the outer folds to all records, then averaged and thresholded the three continuous GCM projections. The resulting increases ranged from 7.1% to 21.6%; each individual GCM also projected a gain. Compared with the QP model fitted to the same full dataset, the four configurations gave current-map Jaccard indices of 0.733–0.876 and suitable areas that were 0.8%–23.7% smaller (Table S3 in Online Resource 1).

3.4 GCM agreement and environmental extrapolation

All three GCMs projected net gains in every scenario and period (Table 5; Fig. 7). Under SSP5-8.5 at the end of the century, suitable area increased by 8.8%, 18.6% and 16.1% relative to the current baseline for GFDL-ESM4, IPSL-CM6A-LR and MRI-ESM2-0, respectively, giving areas of approximately 1,998,200–2,178,400 km². Binary predictions disagreed over 335,400 km², or 14.84% of the union of suitable areas, mainly in projected gain and loss areas. Pairwise correlations of the continuous predictions were at least 0.967 across the national domain and at least 0.823 within the union of future suitable areas.

Under SSP5-8.5 at the end of the century, 93,958 km² had negative MESS in at least one GCM, with 10,952 km² overlapping future suitable area (Fig. S3 in Online Resource 1). Removing these cells from the future suitable area only reduced the ensemble increase from 15.91% to 15.31%. Applying the nationally referenced common-support mask to both current and future maps gave an increase of 18.51% relative to the masked current suitable area. Negative MESS mainly corresponded to BIO11 and BIO15 values outside the current environmental range. Approximately 1.715 million km² remained suitable in all 18 future combinations, representing 93.4% of current suitable area. The GCMs agreed most closely in the main southern suitability belt, with disagreement concentrated along the northern and coastal margins.

3.5 National and M500 calibration domains

The M500 model had a weighted spatial AUC of 0.735 and pooled MTSPS omission of 40.7%. Its current prediction surface had a correlation of 0.921 and a Jaccard index of 0.879 against the national model, and its suitable area was 6.32% smaller (Fig. S7 in Online Resource 1).

Under SSP5-8.5 at the end of the century, the M500 model projected an 18.0% increase in suitable area across the national projection domain and a 17.9% increase within the M500 geographical domain. The paired current–future common-support comparison using M500-referenced MESS gave an increase of 20.8%. Baseline areas and threshold definitions for the reporting domains are given in Methods S2 and Table S4 of Online Resource 1.

4 Discussion

4.1 Environmental associations of current suitability

The main suitability belt of *A. prolongatum* extends through humid mountains from southwestern to southeastern China, consistent with its documented occurrence on forest tree trunks and moist rock surfaces (Lin and Viane 2013). Highly suitable patches are unevenly distributed within the belt. The fern is classified as a facultative epiphyte in Taiwan, China (Hsu and Wolf 2009). Both trunks and rock surfaces can support the fern, but they may differ in water retention and thermal buffering.

Of the five predictors, mean temperature of the coldest quarter had the highest contribution and permutation importance. Precipitation seasonality and precipitation of the driest quarter also made substantial contributions. Moisture affects fern gametophyte growth and reproduction (Krieg and Chambers 2022). In experiments on the congener *Asplenium scolopendrium* var. *americanum*, Testo and Watkins (2013) found that gametophytes were sensitive to desiccation and that higher growing temperatures inhibited gametophyte growth and sporophyte formation. Whether *A. prolongatum* responds similarly remains to be tested. Elevation had a low percentage contribution but relatively high permutation importance, indicating that the measures capture different aspects of its predictive role.

The Shitai and Qimen collection localities both lie within predicted suitable patches in southern Anhui and provide locality references for the regional predictions. Forest types and substrates can then be used to select field sites within these patches.

4.2 Temperature and moisture context of future changes

Gains at the northern margin and local losses in the south occurred in the same set of climate projections. Given the role of mean temperature of the coldest quarter in the model, the northern gains are consistent with a possible relaxation of winter cold constraints. The projected losses in southern lowlands, on Hainan and along the coast suggest that a nationwide gain need not mean that temperature and moisture conditions become more favourable everywhere.

Local losses in the south may reflect concurrent changes in temperature and precipitation seasonality. The northward shift of the suitable-area centroid broadly agrees with the direction of range shifts observed under climate warming (Chen et al. 2011). Whether the fern can occupy newly suitable

sites also depends on forest connectivity, substrate and dispersal. Recording forest humidity and substrate conditions in northern gain areas and southern loss areas could help assess whether these regional differences are detectable in the field.

4.3 Prediction agreement and spatial differences

The fixed-QP and nested evaluations gave similar spatial AUCs and both had higher omission in the northern folds. The different feature combinations selected across folds show that parameter choice varied with the spatial composition of the training records. The main southwest-to-southeast suitability belt persisted when models used the E1+E2 subset, 20-km thinning or target-group backgrounds, with larger differences along its edges. Additional occurrence records there would help test the predictions at the margins.

By the end of the century, projected suitable-area gains ranged from 8.8% to 18.6% across GCMs and from 15.9% to 26.0% across thresholds applied to the ensemble surface. The comparisons agreed on the direction of net change but differed in its size and in the positions of gains and losses. The main southern suitability belt was comparatively stable across scenarios. Climate-model disagreement and some areas of environmental extrapolation occurred along the changing margins. Suitable area still increased after negative-MESS cells were excluded, but the locations of patches along the margins warrant field checks.

4.4 Calibration domain and study limitations

A national domain is practical for resource surveys in China, but national borders do not represent historical accessibility (Barve et al. 2011). Calibrating within M500 changed the selected parameters, estimated current suitable area and spatial evaluation. Because AUC depends on the composition of the background, the lower AUC for M500 does not tell us which domain better reflects dispersal history (Lobo et al. 2008). We used the national model for mapping and M500 to assess sensitivity to background extent. The two projections broadly overlapped within the main suitability belt. Cross-border records and geographical connectivity could help explain differences along its edges.

Nested evaluation selected model complexity within a fixed predictor set, without repeating predictor selection in each fold. The three GCMs cover only part of climate-model variation, and occurrence dates do not fully match the climate baseline. At approximately 5-km resolution, the model does not resolve bark water retention, lithology or canopy humidity. Recording these conditions in projected gain, loss and disagreement areas would help relate regional suitability to occupied microhabitats.

5 Conclusions

Under the fitted model and future climate scenarios considered, the main potential suitability belt for *A. prolongatum* remains in the humid mountains of southern China. Some northern patches became suitable in the projections, but spatial holdouts missed more records in the north; these patches are candidates for surveys. In southern Anhui, resurveys can start at the Shitai and Qimen specimen localities, using canopy humidity and growth substrates to select field sites in nearby predicted patches.

Statements and Declarations

Author contributions

Conceptualization and writing – original draft: Xinyi Liu; methodology, software, data curation, formal analysis and visualization: Jinchuan Guo; investigation: Jinchuan Guo, Wanbo Xing, Yan Zhang and Xiao-su Xiang; writing – review and editing: Xinyi Liu and Qingshan Yang; supervision: Qingshan Yang.

Funding

This research received no specific grant from funding agencies in the public, commercial or not-for-profit sectors.

Data availability

Occurrence records, the all-years GBIF extract with query metadata, predictor sources, model evaluation and sensitivity results are provided in Online Resource 2. Analysis scripts, software records, fitted-model coefficients and current and future prediction surfaces are provided in Online Resource 3. Environmental source rasters can be obtained from the providers and file locations listed in Online Resource 2.

Competing interests

The authors declare no competing interests.

Supplementary information

Online Resource 1: Supplementary Methods S1–S3, Tables S1–S4 and Fig. S1–S8, covering model configurations, threshold sources, M500 reporting extents, software implementations, sensitivity results, response curves, jackknife results and maps.

Online Resource 2: Supplementary Data 1, comprising a 39-worksheet workbook on occurrence provenance, Anhui specimens, predictor selection, calibration and evaluation, future projections

and sensitivity analyses; raw GBIF records, source attribution, environmental-source documentation and future-file manifests.

Online Resource 3: Supplementary Data 2, comprising analysis scripts and dependencies, model inputs, software records, fitted-model coefficients, current and future prediction surfaces, and a script for reproducing area and spatial-evaluation summaries.

References

Barve N, Barve V, Jiménez-Valverde A, Lira-Noriega A, Maher SP, Peterson AT et al (2011) The crucial role of the accessible area in ecological niche modeling and species distribution modeling. *Ecological Modelling 222*:1810–1819. https://doi.org/10.1016/j.ecolmodel.2011.02.011

Boria RA, Olson LE, Goodman SM, Anderson RP (2014) Spatial filtering to reduce sampling bias can improve the performance of ecological niche models. *Ecological Modelling 275*:73–77. https://doi.org/10.1016/j.ecolmodel.2013.12.012

Boucher O, Servonnat J, Albright AL, Aumont O, Balkanski Y, Bastrikov V et al (2020) Presentation and evaluation of the IPSL-CM6A-LR climate model. *Journal of Advances in Modeling Earth Systems 12*:e2019MS002010. https://doi.org/10.1029/2019MS002010

Boyce MS, Vernier PR, Nielsen SE, Schmiegelow FKA (2002) Evaluating resource selection functions. *Ecological Modelling 157*:281–300. https://doi.org/10.1016/S0304-3800(02)00200-4

Brun P, Zimmermann NE, Hari C, Pellissier L, Karger DN (2022) Global climate-related predictors at kilometer resolution for the past and future. *Earth System Science Data 14*:5573–5603. https://doi.org/10.5194/essd-14-5573-2022

Chen IC, Hill JK, Ohlemüller R, Roy DB, Thomas CD (2011) Rapid range shifts of species associated with high levels of climate warming. *Science 333*:1024–1026. https://doi.org/10.1126/science.1206432

Chinese Virtual Herbarium (2026) National Plant Specimen Resource Center online sharing platform. https://www.cvh.ac.cn/ Accessed 28 August 2026

Cobos ME, Peterson AT, Barve N, Osorio-Olvera L (2019) kuenm: an R package for detailed development of ecological niche models using Maxent. *PeerJ 7*:e6281. https://doi.org/10.7717/peerj.6281

Dormann CF, Elith J, Bacher S, Buchmann C, Carl G, Carré G et al (2013) Collinearity: a review of methods to deal with it and a simulation study evaluating their performance. *Ecography 36*:27–46. https://doi.org/10.1111/j.1600-0587.2012.07348.x

Dunne JP, Horowitz LW, Adcroft AJ, Ginoux P, Held IM, John JG et al (2020) The GFDL earth system model version 4.1 (GFDL-ESM 4.1): overall coupled model description and simulation characteristics. *Journal of Advances in Modeling Earth Systems 12*:e2019MS002015. https://doi.org/10.1029/2019MS002015

Elith J, Kearney M, Phillips S (2010) The art of modelling range-shifting species. *Methods in Ecology and Evolution 1*:330–342. https://doi.org/10.1111/j.2041-210X.2010.00036.x

Elith J, Phillips SJ, Hastie T, Dudík M, Chee YE, Yates CJ (2011) A statistical explanation of MaxEnt for ecologists. *Diversity and Distributions 17*:43–57. https://doi.org/10.1111/j.1472-4642.2010.00725.x

Eyring V, Bony S, Meehl GA, Senior CA, Stevens B, Stouffer RJ et al (2016) Overview of the Coupled Model Intercomparison Project Phase 6 (CMIP6) experimental design and organization. *Geoscientific Model Development 9*:1937–1958. https://doi.org/10.5194/gmd-9-1937-2016

Fick SE, Hijmans RJ (2017) WorldClim 2: new 1-km spatial resolution climate surfaces for global land areas. *International Journal of Climatology 37*:4302–4315. https://doi.org/10.1002/joc.5086

GBIF.org (2026) GBIF Species API: *Asplenium prolongatum*, taxon key 4256698. https://api.gbif.org/v1/species/4256698 Accessed 14 August 2026. Occurrence-search API query template: https://api.gbif.org/v1/occurrence/search?taxon_key=4256698&has_coordinate=true&limit=300&offset=0 Accessed 14 August 2026

Guisan A, Thuiller W (2005) Predicting species distribution: offering more than simple habitat models. *Ecology Letters 8*:993–1009. https://doi.org/10.1111/j.1461-0248.2005.00792.x

Guo J, Sun Y, Zhang X, Zhang W, Lian L, Sun J et al (2026) Climate-driven habitat redistribution and conservation gaps of the medicinal fern *Sceptridium ternatum* in China. *Biology 15*:1268. https://doi.org/10.3390/biology15151268

Hirzel AH, Le Lay G, Helfer V, Randin C, Guisan A (2006) Evaluating the ability of habitat suitability models to predict species presences. *Ecological Modelling 199*:142–152. https://doi.org/10.1016/j.ecolmodel.2006.05.017

Horn BKP (1981) Hill shading and the reflectance map. *Proceedings of the IEEE 69*:14–47. https://doi.org/10.1109/PROC.1981.11918

Hsu R, Wolf JHD (2009) Diversity and phytogeography of vascular epiphytes in a tropical–subtropical transition island, Taiwan. *Flora 204*:612–627. https://doi.org/10.1016/j.flora.2008.08.002

International Plant Names Index (2026) *Asplenium prolongatum* Hook. https://www.ipni.org/n/17304410-1 Accessed 14 August 2026

Karger DN, Conrad O, Böhner J, Kawohl T, Kreft H, Soria-Auza RW et al (2021) Climatologies at high resolution for the earth's land surface areas. Version 2.1. EnviDat. https://doi.org/10.16904/envidat.228

Krieg CP, Chambers SM (2022) The ecology and physiology of fern gametophytes: a methodological synthesis. *Applications in Plant Sciences 10*:e11464. https://doi.org/10.1002/aps3.11464

Lin YX, Viane R (2013) Aspleniaceae. In: Wu ZY, Raven PH, Hong DY (eds) Flora of China, vols 2–3 (Pteridophytes). Science Press, Beijing, and Missouri Botanical Garden Press, St. Louis, pp 267–316. https://www.iplant.cn/foc/pdf/Aspleniaceae.pdf

Lobo JM, Jiménez-Valverde A, Real R (2008) AUC: a misleading measure of the performance of predictive distribution models. *Global Ecology and Biogeography 17*:145–151. https://doi.org/10.1111/j.1466-8238.2007.00358.x

Merow C, Smith MJ, Silander JA Jr (2013) A practical guide to MaxEnt for modeling species' distributions: what it does, and why inputs and settings matter. *Ecography 36*:1058–1069. https://doi.org/10.1111/j.1600-0587.2013.07872.x

Muscarella R, Galante PJ, Soley-Guardia M, Boria RA, Kass JM, Uriarte M et al (2014) ENMeval: an R package for conducting spatially independent evaluations and estimating optimal model complexity for Maxent ecological niche models. *Methods in Ecology and Evolution 5*:1198–1205. https://doi.org/10.1111/2041-210X.12261

National Specimen Information Infrastructure (2026) NSII specimen resource platform. https://www.nsii.org.cn/ Accessed 28 August 2026

O'Neill BC, Tebaldi C, van Vuuren DP, Eyring V, Friedlingstein P, Hurtt G et al (2016) The Scenario Model Intercomparison Project (ScenarioMIP) for CMIP6. *Geoscientific Model Development 9*:3461–3482. https://doi.org/10.5194/gmd-9-3461-2016

Parmesan C, Yohe G (2003) A globally coherent fingerprint of climate change impacts across natural systems. *Nature 421*:37–42. https://doi.org/10.1038/nature01286

Phillips SJ, Anderson RP, Schapire RE (2006) Maximum entropy modeling of species geographic distributions. *Ecological Modelling 190*:231–259. https://doi.org/10.1016/j.ecolmodel.2005.03.026

Phillips SJ, Dudík M, Elith J, Graham CH, Lehmann A, Leathwick J et al (2009) Sample selection bias and presence-only distribution models: implications for background and pseudo-absence data. *Ecological Applications 19*:181–197. https://doi.org/10.1890/07-2153.1

Plants of the World Online (2026) *Asplenium prolongatum* Hook. Royal Botanic Gardens, Kew. https://powo.science.kew.org/taxon/urn:lsid:ipni.org:names:17304410-1 Accessed 14 August 2026

Roberts DR, Bahn V, Ciuti S, Boyce MS, Elith J, Guillera-Arroita G et al (2017) Cross-validation strategies for data with temporal, spatial, hierarchical, or phylogenetic structure. *Ecography 40*:913–929. https://doi.org/10.1111/ecog.02881

Royal Botanic Gardens, Kew (2026) *Asplenium prolongatum* Hook. Medicinal Plant Names Services. https://mpns.science.kew.org/mpns-portal/plantDetail?dbs=wcsCmp&plantId=3146113 Accessed 15 November 2026.

Testo WL, Watkins JE Jr (2013) Understanding mechanisms of rarity in pteridophytes: competition and climate change threaten the rare fern *Asplenium scolopendrium* var. *americanum* (Aspleniaceae). *American Journal of Botany 100*:2261–2270. https://doi.org/10.3732/ajb.1300150

Warren DL, Seifert SN (2011) Ecological niche modeling in Maxent: the importance of model complexity and the performance of model selection criteria. *Ecological Applications 21*:335–342. https://doi.org/10.1890/10-1171.1

Weigand A, Abrahamczyk S, Aubin I, Bita-Nicolae C, Bruelheide H, Carvajal-Hernández CI et al (2020) Global fern and lycophyte richness explained: how regional and local factors shape plot richness. *Journal of Biogeography 47*:59–71. https://doi.org/10.1111/jbi.13782

WorldClim (2026) WorldClim v2.1 elevation data. https://www.worldclim.org/data/worldclim21.html Accessed 28 October 2026

Yukimoto S, Kawai H, Koshiro T, Oshima N, Yoshida K, Urakawa S et al (2019) The Meteorological Research Institute earth system model version 2.0, MRI-ESM2.0: description and basic evaluation of the physical component. *Journal of the Meteorological Society of Japan. Ser. II 97*:931–965. https://doi.org/10.2151/jmsj.2019-051

Table 1 Occurrence-record processing and sensitivity datasets

Stage	Records	Analytical use
Union of coordinates from multiple sources	301	GBIF, CVH, NSII, vouchers, floristic sources and literature
After quality control	287	Exclusion rules in Online Resource 2
One record per 2.5 arc-min cell	246	Main dataset; all Anhui coordinates excluded
E1: specimen or image evidence	58	Main dataset and occurrence-evidence sensitivity analysis
E2: traceable voucher or catalogue number	53	Main dataset and occurrence-evidence sensitivity analysis
E4: curated coordinate records	135	Name, duplicate/conflict, geographical and grid checks passed
E1+E2 subset	111	Occurrence-evidence sensitivity analysis; dates 1980–2026
20-km thinning	168	Stronger spatial-thinning sensitivity analysis
Non-target fern background	194,689	Sampling-effort surfaces with σ = 6, 12 and 24 cells

Note: Evidence-category codes follow Online Resource 2. E3 denotes database records with a species name and coordinates but no linked material evidence; no E3 records occurred in the main dataset.

Table 2 Final predictors and their treatment in future projections

Code	Description	Source	Future treatment
BIO11	Mean temperature of the coldest quarter (°C)	CHELSA v2.1	Dynamic CHELSA CMIP6 layer
BIO15	Precipitation seasonality (%)	CHELSA v2.1	Dynamic CHELSA CMIP6 layer
BIO17	Precipitation of the driest quarter (mm)	CHELSA v2.1	Dynamic CHELSA CMIP6 layer
Elevation	Elevation (m)	WorldClim v2.1	Static; model-structure sensitivity analysis
Slope	Slope (degrees)	WGS84 DEM; Horn 3 × 3 algorithm with a fixed conversion of 111,000 m per degree	Static; latitude-corrected check

Table 3 Model evaluation results

Evaluation	RM/FC	n	AUC	MTSPS omission	P10 omission	Boyce
Outer fold 1: southwest	1.5/LT	47	0.908	14.9%	34.0%	0.813
Outer fold 2: southeast	0.5/P	76	0.936	9.2%	9.2%	0.813
Outer fold 3: northwest	0.1/LQ	76	0.863	18.4%	55.3%	0.500
Outer fold 4: northeast	2/QPT	47	0.896	27.7%	42.6%	0.813
Nested spatial summary	Varies	246	0.900 weighted	16.7% pooled	34.6% pooled	0.734 mean
Fixed-QP spatial diagnostic	2/QP	246	0.898 weighted	13.0% pooled	29.3% pooled	—
Random tenfold diagnostic	2/QP	246	0.922 ± 0.021	2.4% ± 3.4%	—	—

Note: Spatial summaries report test-sample-size-weighted AUC and pooled omission rates. The random-tenfold row reports means ± standard deviations across folds; individual spatial-fold rows report held-out test results. A dash indicates that the metric is not reported in this table. Boyce denotes the grouped Boyce index; Varies denotes fold-specific RM/FC selection. FC, feature classes.

Table 4 Current macroenvironmental suitability classes

Class	Logistic suitability score p	Approximate area (km²)	Share of valid domain (%)
Unsuitable	$p < 0.2116$	7,508,400	80.35
Low suitability	$0.2116 \leq p < 0.4744$	1,257,100	13.45
Moderate suitability	$0.4744 \leq p < 0.7372$	541,900	5.80
High suitability	$p \geq 0.7372$	37,000	0.40

Table 5 Percentage changes in suitable area for the three GCMs and continuous-surface ensemble, relative to the current area of 1,836,000 km²

SSP	Period	GFDL-ESM4	IPSL-CM6A-LR	MRI-ESM2-0	Continuous-surface ensemble
SSP1-2.6	2011–2040	+0.8	+4.3	+2.5	+2.5
SSP1-2.6	2041–2070	+6.0	+6.9	+7.5	+6.8
SSP1-2.6	2071–2100	+5.7	+6.1	+8.5	+6.9
SSP5-8.5	2011–2040	+1.1	+4.2	+3.1	+2.8
SSP5-8.5	2041–2070	+6.6	+10.3	+9.2	+8.8
SSP5-8.5	2071–2100	+8.8	+18.6	+16.1	+15.9

Fig. 1

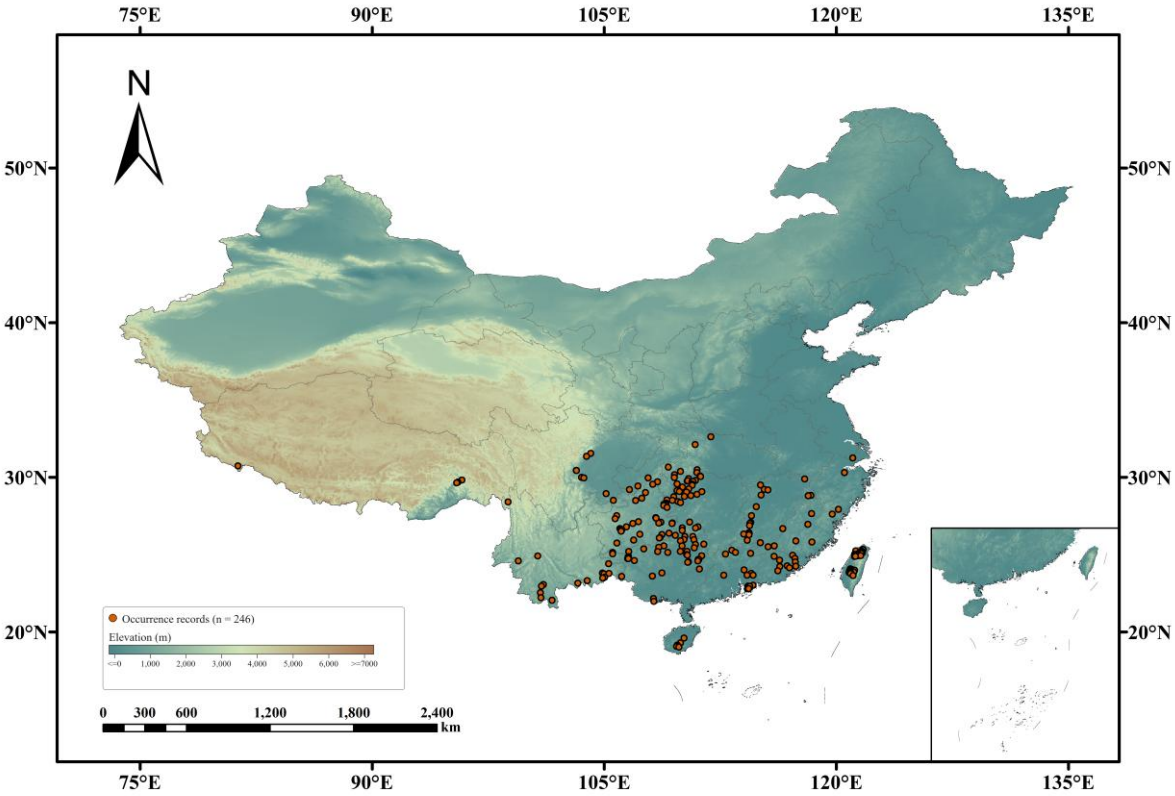

75°E
90°E
105°E
120°E
135°E
N
50°N
40°N
30°N
20°N
Occurrence records (n = 246)
Elevation (m)
<=0
1,000
2,000
3,000
4,000
5,000
6,000
>=7000
0
300
600
1,200
1,800
2,400
km

Fig. 2

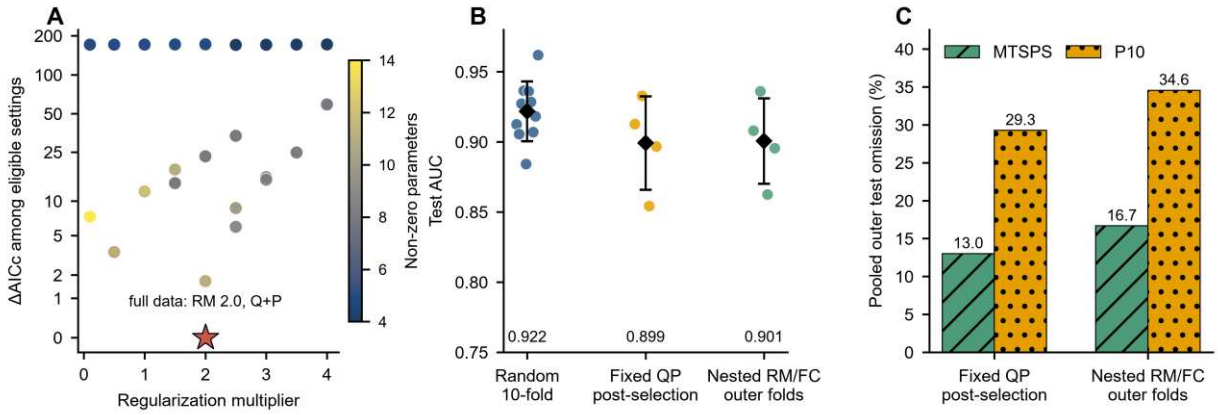

A
ΔAICc among eligible settings
200
100
50
25
10
5
2
1
0
full data: RM 2.0, Q+P
0
1
2
3
4
Regularization multiplier
14
12
10
8
6
4
Non-zero parameters
B
Test AUC
0.95
0.90
0.85
0.80
0.75
0.922
0.899
0.901
Random 10-fold
Fixed QP post-selection
Nested RM/FC outer folds
C
MTSPS
P10
Pooled outer test omission (%)
40
35
30
25
20
15
10
5
0
13.0
29.3
16.7
34.6
Fixed QP post-selection
Nested RM/FC outer folds

Fig. 3

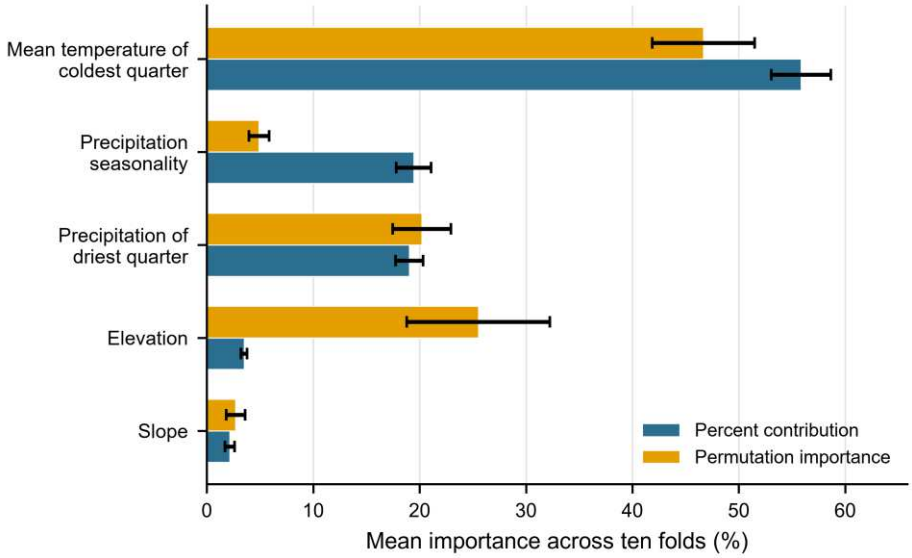

Mean temperature of coldest quarter
Precipitation seasonality
Precipitation of driest quarter
Elevation
Slope
Percent contribution
Permutation importance
0
10
20
30
40
50
60
Mean importance across ten folds (%)

Fig. 4

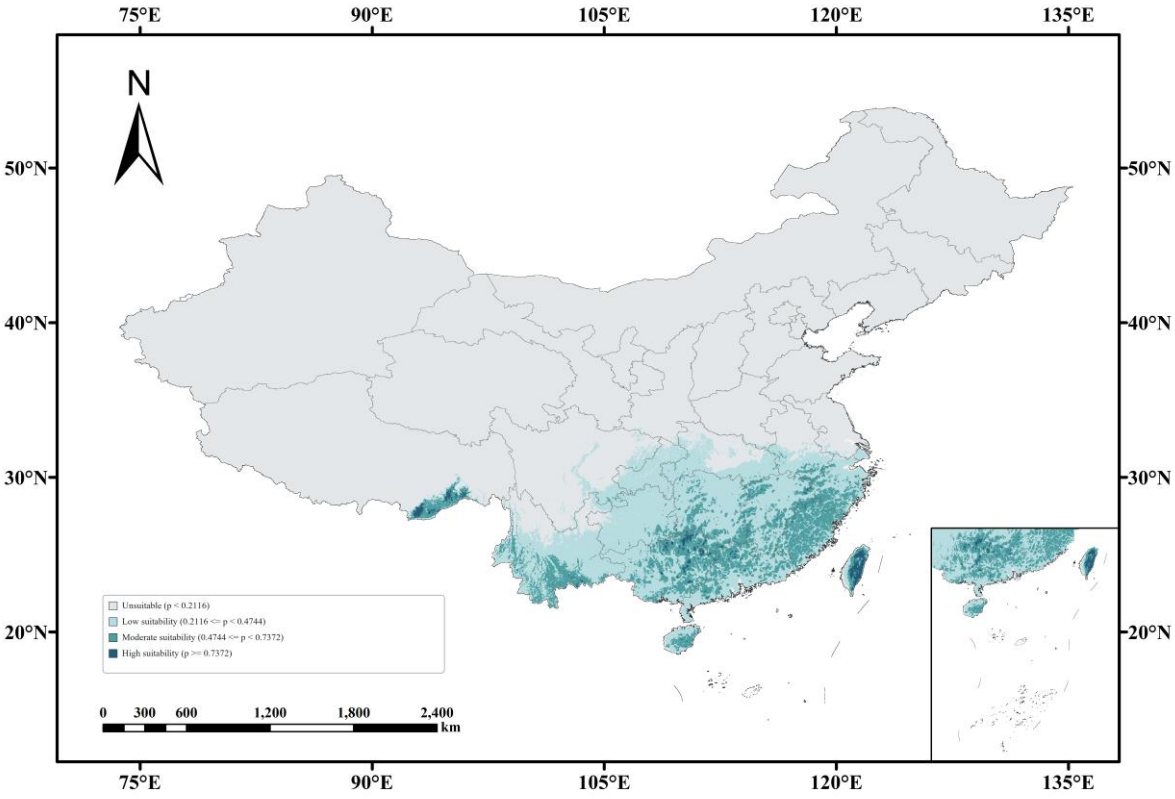

75°E
90°E
105°E
120°E
135°E
N
50°N
40°N
30°N
20°N
Unsuitable (p < 0.2116)
Low suitability (0.2116 <= p < 0.4744)
Moderate suitability (0.4744 <= p < 0.7372)
High suitability (p >= 0.7372)
0 300 600 1,200 1,800 2,400
km

Fig. 5

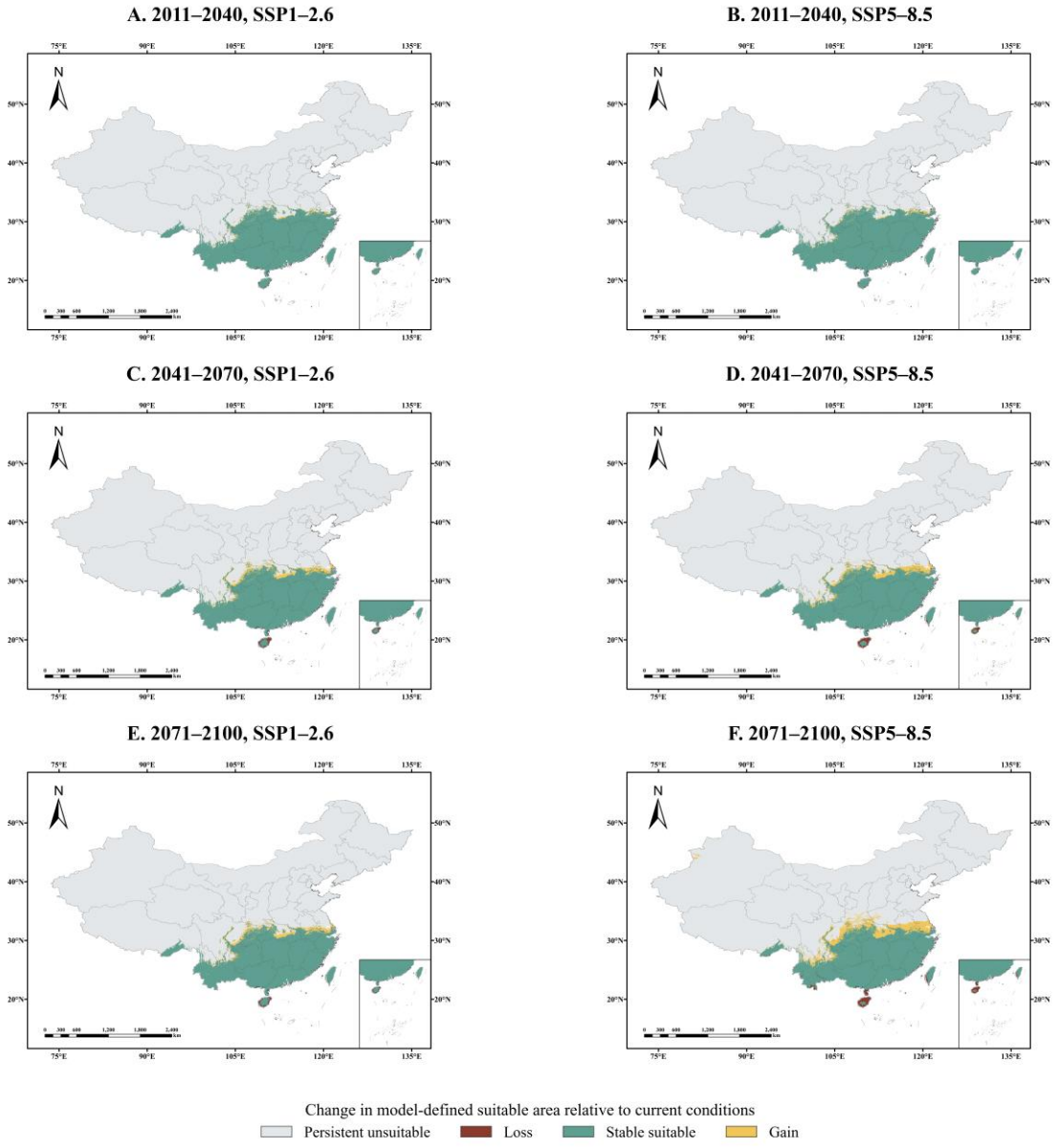

A. 2011–2040, SSP1–2.6
B. 2011–2040, SSP5–8.5
C. 2041–2070, SSP1–2.6
D. 2041–2070, SSP5–8.5
E. 2071–2100, SSP1–2.6
F. 2071–2100, SSP5–8.5
Change in model-defined suitable area relative to current conditions
Persistent unsuitable
Loss
Stable suitable
Gain

Fig. 6

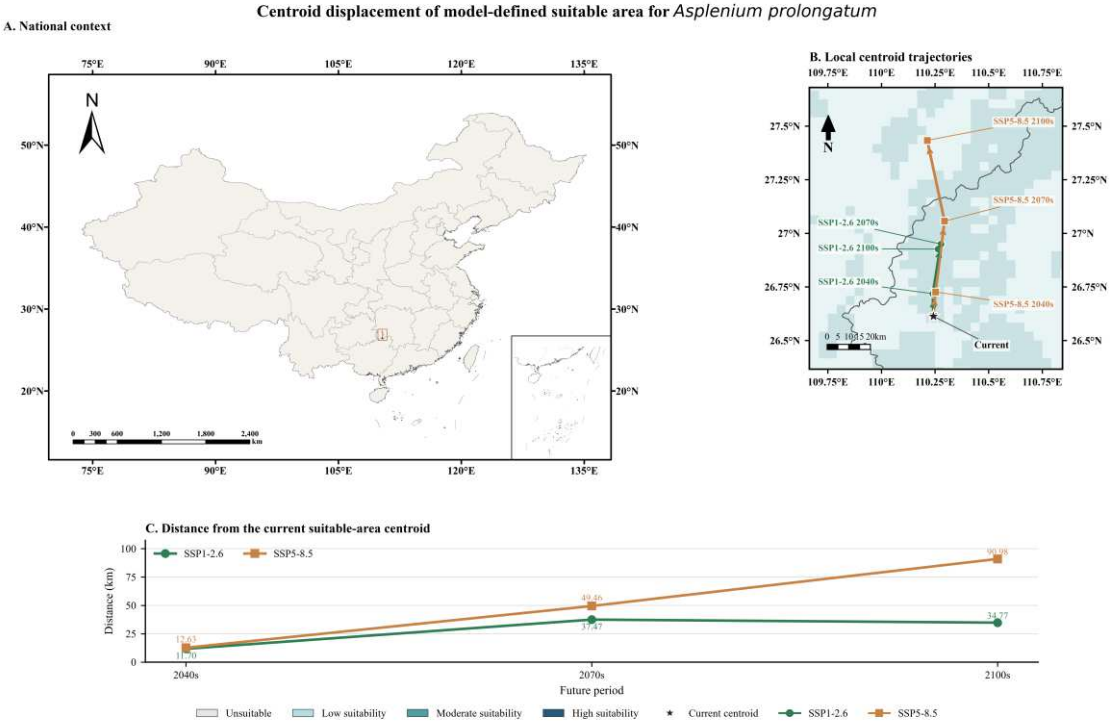

Centroid displacement of model-defined suitable area for Asplenium prolongatum
A. National context
B. Local centroid trajectories
SSP5-8.5 2100s
SSP5-8.5 2070s
SSP1-2.6 2070s
SSP1-2.6 2100s
SSP1-2.6 2040s
SSP5-8.5 2040s
Current
C. Distance from the current suitable-area centroid
SSP1-2.6
SSP5-8.5
Distance (km)
12.63
11.70
49.46
37.47
99.98
34.37
2040s
2070s
2100s
Future period
Unsuitable
Low suitability
Moderate suitability
High suitability
Current centroid
SSP1-2.6
SSP5-8.5

Fig. 7

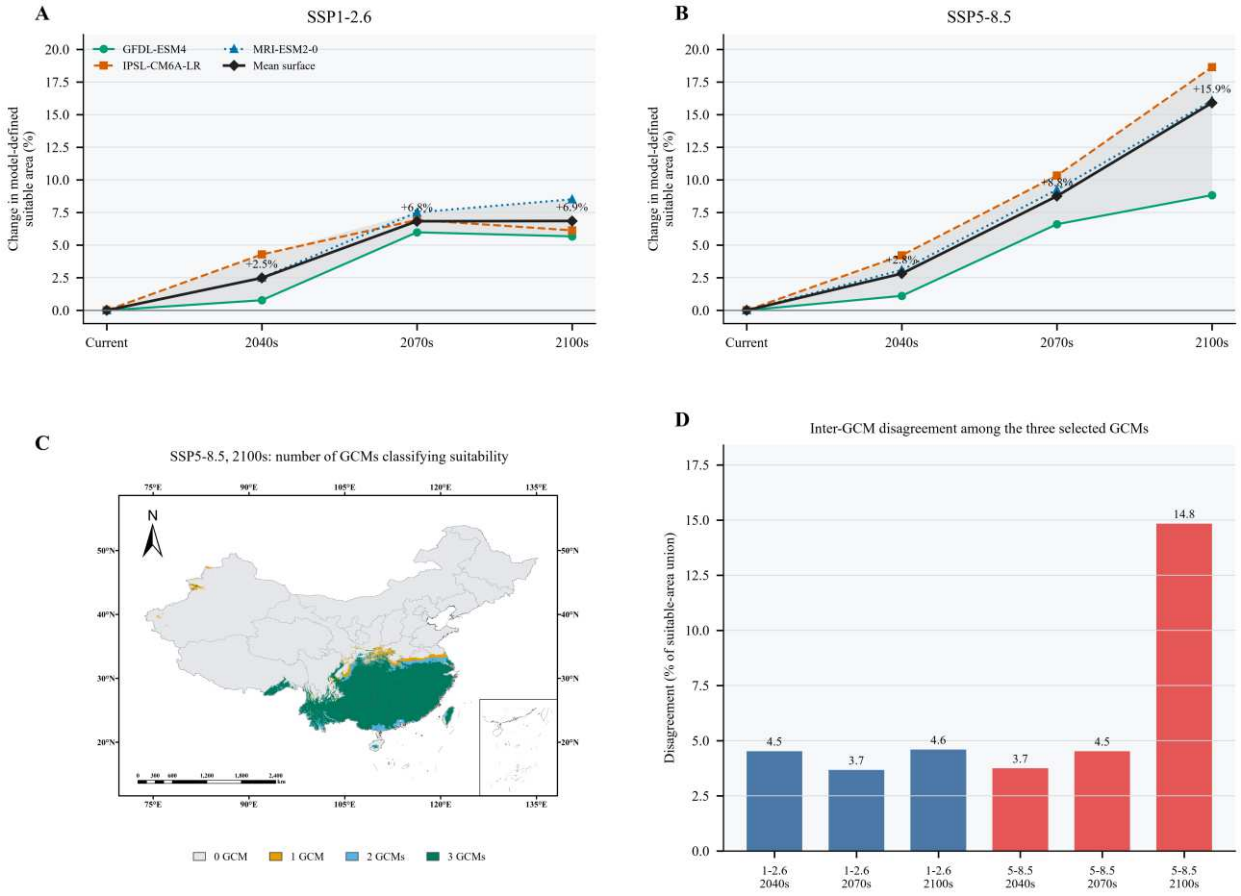

A
SSP1-2.6
GFDL-ESM4
IPSL-CM6A-LR
MRI-ESM2-0
Mean surface
Change in model-defined suitable area (%)
+2.5%
+6.8%
+6.9%
Current
2040s
2070s
2100s
B
SSP5-8.5
+15.9%
C
SSP5-8.5, 2100s: number of GCMs classifying suitability
N
0 GCM
1 GCM
2 GCMs
3 GCMs
D
Inter-GCM disagreement among the three selected GCMs
Disagreement (% of suitable-area union)
4.5
3.7
4.6
3.7
4.5
14.8
1-2.6 2040s
1-2.6 2070s
1-2.6 2100s
5-8.5 2040s
5-8.5 2070s
5-8.5 2100s

Figure captions

Fig. 1 The 246 modelling records and elevation of the study area. The lower-right inset shows the South China Sea islands. Cartographic layers follow Guo et al. (2026)

Fig. 2 Full-dataset parameter selection and spatial evaluation. (A) ΔAICc of models passing pROC and omission screening; colour indicates the number of non-zero parameters, and the star marks the selected model. Vertical positions use log10(ΔAICc + 1), with tick labels showing the original ΔAICc values. (B) Test AUC from random tenfold, fixed-QP spatial and outer nested spatial evaluations. Points show individual folds; black diamonds and error bars show arithmetic means ± standard deviations across folds. Spatial AUC means in this panel are unweighted, whereas Table 3 reports test-sample-size-weighted spatial AUC. (C) Pooled omission rates for fixed-QP and outer nested spatial evaluations, with distinct patterns for MTSPS and P10 thresholds

Fig. 3 Mean percentage contributions and permutation importance of the five predictors across 10 folds. Error bars represent ±1 standard deviation among folds

Fig. 4 Current macroenvironmental suitability. The corresponding overlay with modelling records is shown in Fig. S4 (Online Resource 1). Cartographic layers follow Guo et al. (2026)

Fig. 5 Stable, lost and newly suitable areas. Current tenfold mean and future three-GCM continuous ensemble surfaces were separately classified at MTSPS = 0.2116, and the resulting binary maps were overlaid to identify change classes. Cartographic layers follow Guo et al. (2026)

Fig. 6 Area-weighted centroids of current and future suitable areas. Lines connect centroid positions across scenarios and periods. Cartographic layers follow Guo et al. (2026)

Fig. 7 Differences among future projections from three GCMs. (A, B) Area changes for individual GCMs and the continuous mean surface. (C) Number of GCMs classifying each cell as suitable under end-century SSP5-8.5. (D) Binary disagreement area as a proportion of the union of suitable areas for each SSP–period combination. Cartographic layers follow Guo et al. (2026)

Supplementary Files

This is a list of supplementary files associated with this preprint. Click to download.

- Supplementaryinformationlegends.docx
- ESM1.pdf
- ESM2.zip
- ESM3.zip